CHEMISTRY OF MATERIALS

Open Access

pubs.acs.org/cm

Article

Synthesis, Structure, and Properties of $CuBiSeCl_2$: A Chalcohalide Material with Low Thermal Conductivity

Published as part of Chemistry of Materials virtual special issue "C. N. R. Rao at 90".

Cara J. Hawkins, Jon A. Newnham, Batoul Almoussawi, Nataliya L. Gulay, Samuel L. Goodwin, Marco Zanella, Troy D. Manning, Luke M. Daniels, Matthew S. Dyer, Tim D. Veal, John B. Claridge, and Matthew J. Rosseinsky*

Cite This: *Chem. Mater.* 2024, 36, 4530–4541

Read Online

ACCESS | Metrics & More | Article Recommendations | Supporting Information

ABSTRACT: Mixed anion halide-chalcogenide materials have recently attracted attention for a variety of applications, owing to their desirable optoelectronic properties. We report the synthesis of a previously unreported mixed-metal chalcohalide material, $CuBiSeCl_2$ (*Pnma*), accessed through a simple, low-temperature solid-state route. The physical structure is characterized through single-crystal X-ray diffraction and reveals significant Cu displacement within the $CuSe_2Cl_4$ octahedra. The electronic structure of $CuBiSeCl_2$ is investigated computationally, which indicates highly anisotropic charge carrier effective masses, and by experimental verification using X-ray photoelectron spectroscopy, which reveals a valence band dominated by Cu orbitals. The band gap is measured to be 1.33(2) eV, a suitable value for solar absorption applications. The electronic and thermal properties, including resistivity, Seebeck coefficient, thermal conductivity, and heat capacity, are also measured, and it is found that $CuBiSeCl_2$ exhibits a low room temperature thermal conductivity of 0.27(4) W K^{-1} m^{-1}, realized through modifications to the phonon landscape through increased bonding anisotropy.

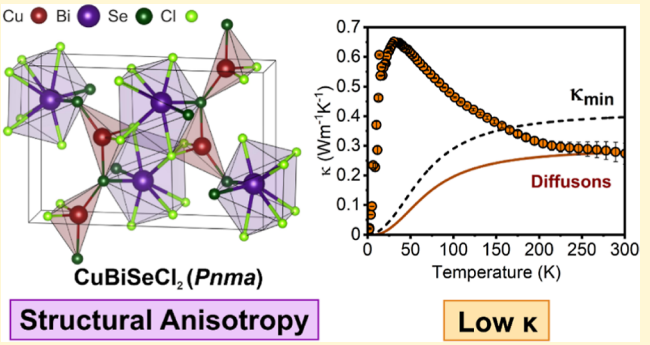

1. INTRODUCTION

Employing a multiple anion approach to material design provides a route to achieving potentially improved properties beyond single anion compositions.[1] In comparison with single-anion materials, mixed-anion compounds are less well characterized. The myriad opportunities afforded through the exploration of novel multianionic phase spaces have recently stimulated more research into this area. Mixed anion chemistry drives material design in two ways: by increasing the number of degrees of freedom available in a system and by modifying the bonding within a material. This can lead to increased structural anisotropy, changes in dimensionality, and the evolution of novel structure types.[2,3] Structural changes arising from such bonding variations facilitate the emergence of new physical phenomena[4−6] and also provide opportunities for optoelectronic property tuning through modifications to the electronic structure.[7,8] A multiple anion approach has already been successfully applied to engineer desirable properties in a variety of energy materials, including battery cathode materials,[9,10] solid-state electrolytes,[11] and thermoelectrics.[12−14]

Halide-chalcogenide, or "chalcohalide", materials are an emerging class of mixed anion materials that contain one or more different metal cations, at least one chalcogenide anion, and at least one halide anion. The multifunctionality of these materials has made them a suitable platform for property tuning to suit a variety of applications, including photocatalysis[15] and X-ray detection.[16] In particular, they have gained attention as potential solar absorbers, with the aim of using a split anion approach[17] to combine the desirable optoelectronic properties of lead halide perovskites (LHPs) with the enhanced stability of chalcogenide-based materials.[18,19] The opportunities for wider compositional and structural exploration through employing the mixed anion chemistry of chalcohalide materials make them a valuable starting point for this task.[20] Several mixed-metal chalcohalides are suitable for photovoltaic (PV) applications, including $Sn_2SbS_2I_3$[21,22] and $CuBiSCl_2$. The latter was recently applied in a single-junction cell by Ming and co-workers and demon-

Received: January 22, 2024
Revised: April 4, 2024
Accepted: April 5, 2024
Published: April 23, 2024

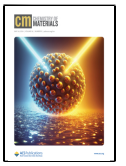

https://doi.org/10.1021/acs.chemmater.4c00188
Chem. Mater. 2024, 36, 4530−4541

strated exceptional environmental stability, a suitable band gap of 1.44 eV, and a PCE of 1%.[23]

Here, we report the synthesis, crystal structure, and thermal, electronic, and optical properties of $CuBiSeCl_2$, a previously unreported mixed-metal chalcohalide material. $CuBiSeCl_2$ is a p-type semiconductor with a low thermal conductivity of 0.27(4) W K^{-1} m^{-1} and a band gap of 1.33(2) eV. The material was also determined to be stable in ambient air for over a month.

2. EXPERIMENTAL SECTION

2.1. Reagents. CuCl (99.999%), Bi_2Se_3 (99.995%), and $BiCl_3$ (99.995%) were purchased from Sigma-Aldrich and were used without further purification. Reagents were stored and handled in an Ar-filled glovebox with <0.1 ppm of O_2 and <0.1 ppm of H_2O.

2.2. Synthesis of $CuBiSeCl_2$. Powder samples of $CuBiSeCl_2$ on a 1 g scale were synthesized by grinding stoichiometric amounts of reagents in an agate mortar, pressing the reagent mix into an 8 mm diameter pellet, and loading into a flame-dried quartz ampule of dimensions 1 cm × 20 cm. The ampule was evacuated to 1×10^{-3} mbar and sealed under a vacuum. The sample was placed horizontally into a high-temperature oven. The sample was then heated using a ramp rate of 5 °C/min, fired at 430 °C for 10 h, and cooled to 200 °C using a ramp rate of 0.1 °C/min before shutting off the oven and allowing it to cool to room temperature. Single crystals of $CuBiSeCl_2$ were grown using the same reaction conditions used for powder synthesis, but a constant cooling rate of 1 °C/h was used between 430 °C and room temperature.

2.3. Powder X-ray Diffraction. Preliminary phase identification was carried out using a Rigaku SmartLab diffractometer with Mo Kα radiation (λ = 0.7107 Å) in the Debye−Scherrer geometry. Samples were sealed inside 0.2 mm diameter borosilicate capillaries in an Ar-filled glovebox. 16 h scans were conducted on a Bruker D8 Advance with monochromatic Cu Kα_1 radiation (λ = 1.54056 Å) in the Debye−Scherrer geometry to obtain high quality data for structural refinement. A LaB_6 internal standard was ground into the $CuBiSeCl_2$ mixture to extract accurate lattice parameters during refinement. 12 hour scans were conducted on an X'Pert Panalytical diffractometer with monochromatic Co Kα_1 radiation (λ = 1.788965 Å) in the Bragg−Brentano geometry to quantify the extent of preferred orientation in pressed pellets of $CuBiSeCl_2$. Rietveld refinements against $CuBiSeCl_2$ powder x-ray diffraction (PXRD) data were conducted using TOPAS Academic V5.[24] The background, lattice parameters, atomic positions, and atomic displacement parameters were refined against the data; a Chebyshev polynomial function was used to model the background; and the peak shapes were modeled using Stephens orthorhombic functions.[25] Structural refinement parameters are available in the Supporting Information (S17).

2.4. Single Crystal X-ray Diffraction. A black single crystal with a platelet shape was selected under a polarizing microscope and then studied by single crystal x-ray diffraction (SCXRD) on beamline I19, Diamond Light Source, Didcot, U.K. using silicon double crystal monochromatic synchrotron radiation (λ = 0.6889 Å, Pilatus 2 M detector).[26] The synchrotron data were collected with the sample at 100 K. Cell refinement and data reduction were performed using Xia[27] and Dials programs.[28] The structure was solved and refined using SHELX-2013,[29] implemented through Olex2.[30] The final residual factors converged to $R1$ = 0.0119 and $wR2$ = 0.0114 for reflections with $I > 2\sigma(I)$. Single crystal solution structure refinement parameters, isotropic and anisotropic thermal displacement parameters, and main bond distances are available in the Supporting Information (S13−S16).

2.5. Compositional Analysis. Scanning electron microscopy (SEM) was performed on a Tescan S8000. Pelletized powder and single crystal samples were attached to an adhesive carbon tape stuck on an aluminum SEM stub. To reduce the charging effects, the samples were coated with a thin layer of carbon. Energy dispersive X-ray (EDX) spectroscopy and wavelength dispersive X-ray (WDX) spectroscopy were performed on the same instrument using X-MaxN and Wave detectors from Oxford Instruments. WDX calibrations for the different elements were obtained by measuring the WDX spectra of appropriate standards. Standard purity was confirmed by using X-ray diffraction and electron microscopy. Quantification was performed by using Aztec software.

2.6. Transmission Electron Microscopy Imaging. Transmission electron microscopy (TEM) images were collected on $CuBiSeCl_2$ particles by using a JEOL JEM 2100+ transmission electron microscope, and compositions were confirmed by using EDX. Samples were loaded onto a Au TEM grid, which was then mounted to a JEOL common specimen holder (EM-21010) before being introduced into the microscope.

2.7. Spark Plasma Sintering. Dense pellets (~88% theoretical density) were obtained by spark plasma sintering (SPS) of the phase-pure $CuBiSeCl_2$ powder at 300 MPa and 270 °C for 5 min in a 10^{-3} mbar vacuum using a commercial Thermal Technology LLC DCS10 furnace. Powder samples (~0.45 g) were pressed in a 10 mm diameter, graphite-foil-lined tungsten carbide die set (with 6% Co binder). Heating and pressure ramp rates were set to 20 °C/min and 100 MPa/min, respectively. The temperature was monitored through a borehole on the side of the die set using a thermocouple. After pressing, the pellets were lightly polished with SiC paper to remove the graphite foil from the pellet surface.

2.8. UV−Vis Spectrometry. Diffuse reflectance of $CuBiSeCl_2$ powder was measured using an Agilent Cary 5000 instrument between 200 and 2500 nm with a step size of 1 nm. Calibration to 100 and 0% reflectance was performed prior to measurement using a PTFE standard and a light trap, respectively. The band gap was determined from a Tauc plot using a method described by Makuła et al.[31]

2.9. X-ray Photoelectron Spectroscopy. Core-level and valence band X-ray photoelectron spectroscopy (XPS) measurements were collected at HarwellXPS, Didcot, U.K. XPS analysis was performed using a Kratos Axis SUPRA XPS fitted with a monochromatic Al Kα X-ray source ($h\nu$ = 1486.6 eV), a spherical sector analyzer, and 3 multichannel resistive plates, 128 channel delay line detectors. All data were recorded at 150 W and a spot size of 700 × 300 μm^2. Survey scans were recorded at a pass energy of 160 eV, and high-resolution scans were recorded at a pass energy of 20 eV. Electronic charge neutralization was achieved using a magnetic immersion lens. All sample data were recorded at a pressure below 10^{-8} Torr and temperature of 294 K. Data were analyzed using CasaXPS v2.3.19PR1.0. Peaks were fit with a Shirley background prior to component analysis. Mixed Gaussian−Lorentzian lineshapes [GL(50)] were used to fit components. All binding energies were measured with respect to the Fermi edge of a Ag foil reference sample.

The ionization potential (IP) of $CuBiSeCl_2$ was determined by collecting the secondary electron cutoff (SEC) region using a monochromatic Al Kα SPECS X-ray source with a PSP Vacuum Technology hemispherical electron energy analyzer with a mean radius of 120 mm. Pass energies of 2 eV for the SEC, 10 eV for core levels, and 50 eV for survey scans were used to measure the emitted photoelectrons. Measurements were performed in an ultrahigh-vacuum chamber with a base pressure of 2×10^{-10} mbar. SEC data were recorded at 16 W to prevent overloading the analyzer. A 10 V bias was applied to the sample to remove any effects from the material work function. The Cu 2p region was also measured to use as a reference. The spectrometer resolution was determined to be 0.40 eV by fitting a Fermi−Dirac function convolved with a Gaussian function to the Fermi edge of the Ag foil.

2.10. Properties Measurement. SPS prepared pellets were cut into semicircles with 1.13 mm thickness and 4.9 mm radius by using a low-speed, diamond-blade saw for Seebeck coefficient, electronic resistivity, and thermal conductivity measurements. Copper electrodes were attached to the pellet using Ag epoxy and left to dry overnight. The offcuts from the pellets were used for powder diffraction and compositional analysis. The thermal conductivity, electronic conductivity, and Seebeck coefficient were measured simultaneously between 2 and 300 K using two probe geometry on a dense pellet of

https://doi.org/10.1021/acs.chemmater.4c00188
Chem. Mater. 2024, 36, 4530−4541

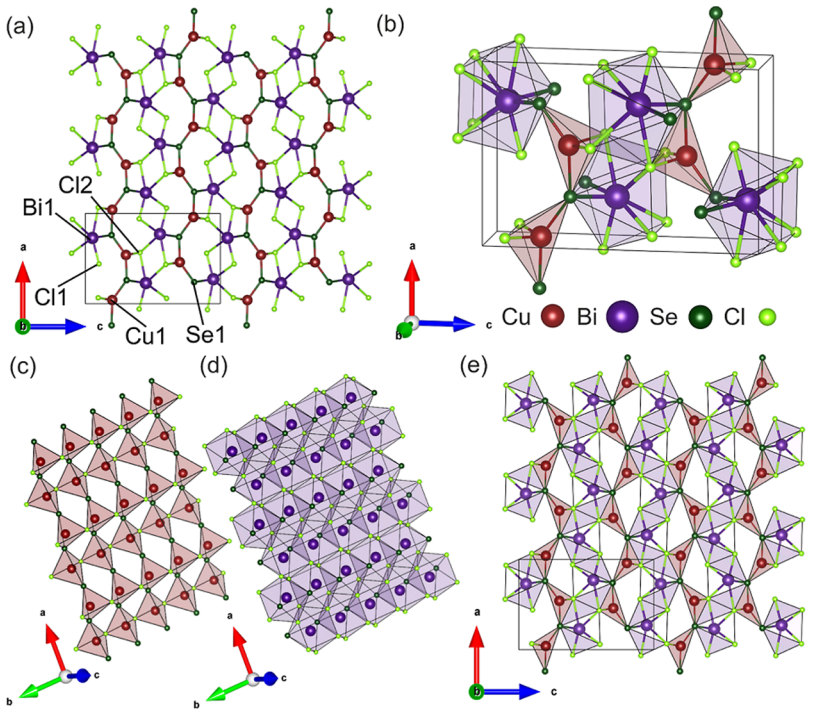

Figure 1. (a) Ball and stick model of the structure of $CuBiSeCl_2$ (*Pnma*) as solved from SCXRD data viewed along the *b* axis and including the unit cell with labeled atomic sites. (b) Unit cell of $CuBiSeCl_2$ depicting bonding environments of $CuSe_2Cl_2$ tetrahedra and $BiSe_2Cl_6$ polyhedra. (c) Layers of $CuSe_2Cl_2$ tetrahedra and (d) $BiSe_2Cl_6$ polyhedra, which are stacked alternately along the *c* direction in $CuBiSeCl_2$. (e) Polyhedral structure of $CuBiSeCl_2$ viewed along the *b* axis.

$CuBiSeCl_2$ using the Thermal Transport Option (TTO) on a Quantum Design physical properties measurement system (PPMS). Heat capacity measurements were performed on a small fragment of dense pellet, with a mass of 0.0125 g, of $CuBiSeCl_2$ using the Heat Capacity Option (HCO) on the PPMS. The sample was mounted using N grease. An addenda measurement was performed on the sample holder and grease prior to mounting and measuring the pellet fragment. Both the addenda and pellet fragment measurements were performed between 2 and 300 K.

2.11. Environmental Stability. The stability of $CuBiSeCl_2$ in ambient air and water was determined as part of this study. The water stability of $CuBiSeCl_2$ was determined by mixing $CuBiSeCl_2$ powder with distilled water for 10 min and pipetting several drops of the suspension onto a glass slide. The slide was then left under ambient conditions for 24 h to allow the water to evaporate. PXRD data were measured before and after water exposure. The air stability was determined by sprinkling $CuBiSeCl_2$ powder onto a glass slide, leaving the slide under ambient conditions for several weeks, and measuring PXRD data at regular time intervals.

2.12. Computational Details. Electronic structure calculations were performed using the periodic density functional theory (DFT) program, Vienna Ab initio simulation package (VASP).[32] Core electrons were treated using the projector-augmented wave approach[33] with Bi 5d electrons included as valence electrons. The hybrid functional, HSE06,[34] was used with the inclusion of spin−orbit coupling (SOC) effects[35] and a plane-wave cut off energy of 400 eV. The structure of $CuBiSeCl_2$ was relaxed until forces fell below 0.01 eV $Å^{-1}$ with a Γ-point centered 10 × 5 × 3 *k*-point grid. The high-symmetry path for calculation of the band structure was obtained using the automatic flow library.[36]

3. RESULTS AND DISCUSSION

Figure 1a represents the crystal structure of $CuBiSeCl_2$ solved from SCXRD data, viewed along the *b* axis. $CuBiSeCl_2$ adopts the orthorhombic symmetry of *Pnma*, with lattice parameters *a* = 8.78415(6) Å; *b* = 3.99803(3) Å; and *c* = 13.13998(9) Å. In this structure, the oxidation states of the species are Cu^+, Bi^{3+}, Se^{2-}, and Cl^-, confirmed with the analysis of core-level binding energies from XPS (S1−S8). The unit cell of $CuBiSeCl_2$ is depicted in Figure 1b and highlights the local bonding environments present in the overall structure. Cu^+ exhibits a coordination number of four, with two Cu−Se bonds and two Cu−Cl bonds forming $CuSe_2Cl_2$ tetrahedra. Bi^{3+} is eight coordinate, forming two Bi−Se bonds and six Bi−Cl bonds to create square antiprismatic $BiSe_2Cl_6$ polyhedra. These copper- and bismuth-centered polyhedra are arranged such that two distinct layers are formed within the structure (Figure 1c,d). Layers of $CuSe_2Cl_2$ tetrahedra, which are connected over common Cl−Cl edges along the *b* direction and share a Se vertex in the *a* direction (Figure 1c), alternate with layers of Bi polyhedra, which face-share along the *b* direction and share two Cl−Cl edges in the *a* direction (Figure 1d). These layers are stacked vertically along the *c* direction such that a single $CuSe_2Cl_2$ tetrahedron is interconnected via edge sharing of two Cl−Se edges with two neighboring $BiSe_2Cl_6$ polyhedra, forming the overall $CuBiSeCl_2$ structure depicted in Figure 1e.

Cu^+ and Bi^{3+} are displaced from the center of their respective environments, visible in Figure 1e. Though it is tetrahedrally coordinated, Cu^+ occupies an octahedral environment created by the Se^{2-} and Cl^- anions. Within this environment, Cu^+ is displaced in the direction of the Cl−Cl octahedral edge to achieve sufficient valence. Bi is then displaced in the direction of the now under-bonded Cl^- at the octahedral corner. The origin of these displacements can be understood through comparisons with known compounds that exhibit similar structures: $CuBiSCl_2$ (*Cmcm*) and $MnBiSe_2Br$ (*Pnma*).

$CuBiSCl_2$ adopts the higher symmetry *Cmcm* space group[40] and exists as a "post-perovskite" structure, first observed in a

https://doi.org/10.1021/acs.chemmater.4c00188
Chem. Mater. 2024, 36, 4530−4541

high-pressure polymorph of $MgSiO_3$.[41] The structure of $CuBiSCl_2$ is made up of alternating layers of CuS_2Cl_4 octahedra and BiS_2Cl_6 polyhedra and shows the same packing of polyhedra as the selenide compound, but the polyhedra are much less distorted in the sulfide analogue. Figure 2 presents a

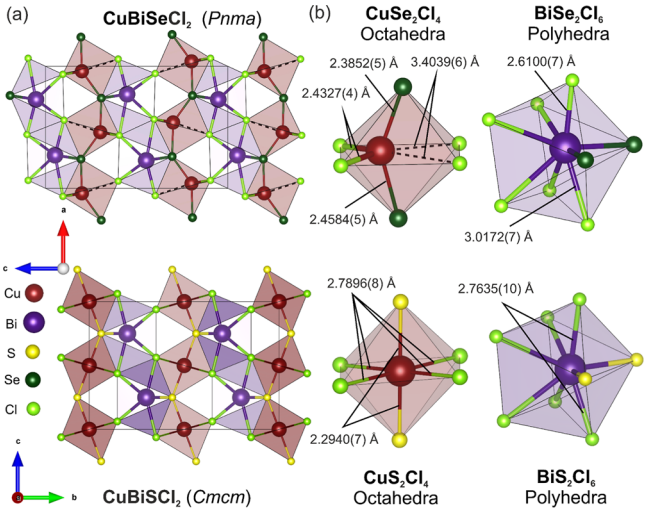

Figure 2. (a) Comparison of the unit cell of $CuBiSeCl_2$ (*Pnma*) viewed along the *b* axis (top) with the unit cell of the higher symmetry $CuBiSCl_2$ (*Cmcm*) viewed along the *a* axis (bottom). To highlight the structural differences between the two materials, Cu is shown in an octahedral environment in $CuBiSeCl_2$, with the longer Cu−Cl bond represented by a dashed line to indicate that this bond is not physically observed. Furthermore, an additional row of $CuSe_2Cl_4$ octahedra are shown to allow for easier comparison of the $CuBiSCl_2$ and $CuBiSeCl_2$ unit cells. (b) Local bonding environments of $CuChCl_4$ octahedra and $BiCh_2Cl_6$ polyhedra (Ch = S, Se) in $CuBiSCl_2$ and $CuBiSeCl_2$ are shown with specific Cu−Cl and Cu−Ch bonds labeled to highlight the variation in bond length with increasing anion size. Fully labeled $CuChCl_4$ octahedra and $BiCh_2Cl_6$ polyhedra can be found in the Supporting Information (S9).

structural comparison of $CuBiSeCl_2$ and $CuBiSCl_2$. Here, octahedral Cu environments are included in the $CuBiSeCl_2$ unit cell and local environments to allow for better comparison between the two materials, though the long Cu−Cl "bonds" [3.4039(6) Å] are shown with dashed lines to indicate they are not physically reasonable. The following discussion will also consider the octahedral $CuSe_2Cl_4$ environment, again for ease of comparison.

The comparison between the structures of $CuBiSeCl_2$ and $CuBiSCl_2$[37] indicates that increasing the chalcogen anion size is the primary driving force for the transition to lower symmetry observed for $CuBiSeCl_2$. A group−subgroup relation scheme detailing the symmetry lowering that occurs between $CuBiSCl_2$ and $CuBiSeCl_2$ is included in the Supporting Information (S10). Figure 2a depicts the unit cells of both structures and Figure 2b shows labeled local bonding environments of $CuBiSeCl_2$ and $CuBiSCl_2$ to highlight the variation in bond lengths between the two materials.

Figure 2b highlights the anisotropic bond lengths present in the $CuSe_2Cl_4$ octahedral environment, with the contracted Cu−Cl bonds in the direction of Cu^+ displacement [2.4327(4) Å] almost 1 Å shorter than the longer Cu−Cl "bonds" opposite [3.4039(6) Å]. The Cu−Se bond lengths also show some anisotropy, though these differences are less pronounced than in the Cu−Cl bond lengths. As the Cu^+ is displaced toward the Cl^- at the octahedral vertex, it is also displaced in the *a* direction toward one of the Se^{2-} species. Figure 2b depicts the shortening of the Cu−Se bond in the direction of displacement [2.3856(9) Å] and the lengthening of the other bond [2.4573(9) Å]. The Cu^+ displacement only happens in the *a*−*c* plane, and there is no displacement along the *b* direction.

Bi^{3+} exhibits the same coordination of six chloride ions and two chalcogen ions in both materials; however, the Cu^+ displacements in $CuBiSeCl_2$ also affect Bi^{3+}, which is displaced from the center of the polyhedra, introducing differences in the Bi−Cl and Bi−Se bond lengths. As shown in Figure 2b, the Bi1−Cl1 bond [2.6100(6) Å] contracts as Bi shifts toward the under-bonded Cl of the $CuSe_2Cl_4$ octahedra, which induces lengthening of the Bi1−Cl2 bond [3.0172(7) Å] opposite. Again, Bi^{3+} displacement happens only in the *a*−*c* plane.

More detail about the origin of Cu^+ displacements in $CuBiSeCl_2$ can be understood using bond valence sum (BVS) analysis (S12−S14). The location of Cu^+ on the 4*a* site at the center of the octahedron in $CuBiSeCl_2$ would yield a BVS of 0.716, indicating that Cu^+ is underbonded in such an environment. Displacement from the center to the 4*c* position toward the Cl−Cl edge achieves higher valence for Cu^+ of 0.913. For comparison, in the reported structure for $CuBiSCl_2$, Cu^+ occupies a site at the center of the octahedron with a BVS of 0.865. The volume of the $CuSe_2Cl_4$ environment increases from 23.8 $Å^3$ in $CuBiSCl_2$ to 33.1 $Å^3$ in $CuBiSeCl_2$, which is the reason the Cu^+ displacement is observed in the latter. This is supported by calculation of BVS maps (Figures S13 and S14) that show a cuboidal region with a side length of ∼0.7 Å about the center of the octahedron where Cu^+ would achieve a valence of 1. Calculation of the BVS parameters for octahedrally coordinated Cu^+ positioned on the 4*c* site in the experimentally observed *Pnma* $CuBiSeCl_2$ material confirms the tetrahedral coordination of Cu^+ by showing that the long Cu−Cl "bond" [3.4039(6) Å] contributes minimally to the overall valence of Cu^+.

We also note that in the structure of $CuBiSCl_2$, a large U_{iso} of 0.068 $Å^2$ is observed for Cu, which may infer some unresolved structural displacement around this position. This is further supported by BVS maps calculated for $CuBiSCl_2$, which depict a cuboidal region of similar size to that observed for $CuBiSeCl_2$.

Considering the coordination chemistry of Cu^+ can also provide insights into the structural displacements present in $CuBiSeCl_2$. Typically, Cu^+ forms 3 and 4-fold coordinate environments. In compounds with similar chemistries to $CuBiSeCl_2$ like Cu_3BiS_3 and $CuIn_xGa_{1-x}Se_2$, Cu^+ preferentially occupies a tetrahedral coordination. In addition to this, Xiao et al. report that, as of yet, there are no reported compounds whereby Cu^+ is 6-fold coordinated with halides.[38]

The crystal structure of $CuBiSeCl_2$ is most similar to that of $MnBiSe_2Br$, which also crystallizes in the space group *Pnma*.[39] A structural comparison between the unit cells of $CuBiSeCl_2$ and $MnBiSe_2Br$ can be found in the Supporting Information (S11). Again, though Cu^+ is tetrahedrally coordinated in $CuBiSeCl_2$, we will consider the $CuSe_2Cl_4$ octahedra for ease of comparison with the $MnSe_4Br_2$ octahedra in $MnBiSe_2Br$.

The structure of $MnBiSe_2Br$ consists of layers of $MnSe_4Br_2$ octahedra and $BiSe_5Br_3$ polyhedra and, like the Cu displacement in $CuBiSeCl_2$, $MnBiSe_2Br$ exhibits a deviation in the position of Mn from the center of the $MnSe_4Br_2$ octahedra and toward the Br−Br octahedral edge. Bi occupies split sites in $MnBiSe_2Br$, with the Bi1 site exhibiting an occupancy of 0.97

https://doi.org/10.1021/acs.chemmater.4c00188
Chem. Mater. 2024, 36, 4530−4541

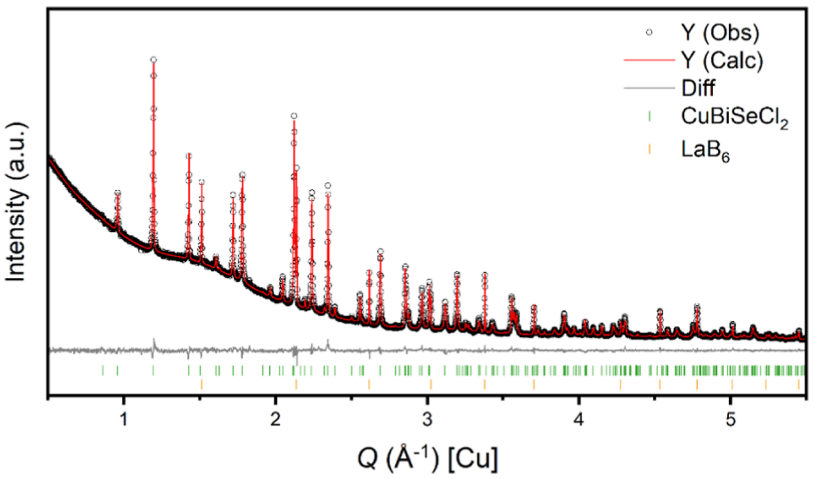

Figure 3. Rietveld analysis of the PXRD data measured for $CuBiSeCl_2$ with LaB_6 used as an internal standard.

and the Bi2 site possessing an occupancy of 0.03. In $CuBiSeCl_2$, the Cu is displaced much more significantly from the center of the octahedra compared to the displacement of Mn observed in $MnBiSe_2Br$. The differences in the cationic displacement magnitude observed in the two structures are partly due to the stoichiometric variation in the local environments, which results in different coordination and bonding.

In the $MnSe_4Br_2$ octahedra, the two Br^- ions occupy equatorial cis positions around the central Mn^{2+} ion with the Se^{2-} ions occupying the remaining four sites (S9). In contrast, in the $CuSe_2Cl_4$ octahedra the four Cl^- ions occupy all equatorial positions and the two Se^{2-} ions are positioned trans on the axial positions. One factor that influences the magnitude of the cationic displacement in $CuBiSeCl_2$ relative to $MnBiSe_2Br$ is the size of the ionic radii in the octahedral environment. In the $MnSe_4Br_2$ environment, all of the anionic species exhibit similar ionic radii (Br 1.96 Å, Se 1.98 Å),[40] which causes minimal displacement of Mn^{2+}. The difference in anion size in the $CuSe_2Cl_4$ octahedra is more significant (Cl 1.81 Å, Se 1.98 Å) and results in a more anisotropic displacement of Cu^+. The variation in structural displacements achieved in these materials by using different coordination environments in three similar structures suggests that using a mixed anion approach provides a route to establishing control over specific structural features.

Rietveld analysis of $CuBiSeCl_2$ PXRD data, shown in Figure 3, was used to confirm the structural model determined from SCXRD data and demonstrate the phase purity of the bulk samples. TEM images (S21) show the particles to be needle-like structures of approximately 1.5 μm × 0.25 μm. Compositional analysis was performed on both single crystal and powder samples of $CuBiSeCl_2$ to corroborate the stoichiometry determined from the single crystal model, as shown in S22–S26. SEM–EDX elemental mapping was performed on a single crystal of $CuBiSeCl_2$ to confirm the homogeneous distribution of elements as well as the absence of oxygen in the structure. Single crystal EDX elemental mapping in Figure S22 indicates that Cu, Bi, Se, and Cl are all uniformly distributed in the sample and the presence of oxygen is minimal. To further confirm the material stoichiometry and account for the significant overlap of Bi^{3+} and Cl^- peaks in the EDX spectra, SEM–EDX and WDX were also measured on $CuBiSeCl_2$ powder, and these data are depicted in S23 and S24. SEM–WDX was used to quantify the Cu/Bi and Bi/Cl ratios, while SEM–EDX measured the Bi/Se ratio. The overall composition of $CuBiSeCl_2$ was determined to be $Cu_{1.10(3)}Bi_{1.0(4)}Se_{1.15(5)}Cl_{2.17(3)}$ consistent with the stoichiometry established from the structural solution.

The band structure and effective masses were calculated for $CuBiSeCl_2$ to provide insights into the optical band gap and mobility of charge carriers within the material as well as elucidate possible applications. The band structure of $CuBiSeCl_2$ is shown in Figure 4a.

The direct band gap calculated from this band structure is found to be 1.5 eV, suggesting that $CuBiSeCl_2$ may have potential as a solar absorber. Interestingly, the calculated direct and indirect bandgaps are very close in energy such that the band gap in $CuBiSeCl_2$ can be considered to be quasi-direct. This occurs since the conduction band in the $\Gamma \rightarrow Z$ direction is extremely flat close to the Γ point and dips slightly as it goes away from the Γ point such that the computed conduction band minimum (CBM) is actually displaced slightly away from the Γ point itself. This leads to an indirect gap that is only very slightly smaller than the direct gap (0.1 meV). This effect is also observed in the band structure of $CuBiSCl_2$, whereby, when SOC is accounted for, the CBM shifts from Y toward Γ, but this energy difference is very small (10 meV); hence, the band gap in this material is considered to be quasi-direct.[23]

To provide insight into the effect of the physical structure on the electronic transport properties in $CuBiSeCl_2$, the band structures of the reported sulfide analogue $CuBiSCl_2$ (*Cmcm*) and the hypothetical, higher-symmetry $CuBiSeCl_2$ (*Cmcm*) material were also calculated (S28). The associated charge carrier effective masses are reported for the experimentally observed $CuBiSeCl_2$ (*Pnma*), the hypothetical higher symmetry $CuBiSeCl_2$ structure (*Cmcm*) and $CuBiSCl_2$ (*Cmcm*) in Table 1. The effective masses for $CuBiSeCl_2$ are reported for the $\Gamma \rightarrow X$, $\Gamma \rightarrow Y$, and $\Gamma \rightarrow Z$ directions. For the *Cmcm* structures, the effective masses are reported for the $Y \rightarrow X_1$, $Y \rightarrow \Gamma$, and $Y \rightarrow T$ reciprocal space paths.

Though the band structure of $CuBiSeCl_2$ exhibits visibly low dispersion, the calculated effective masses within $CuBiSeCl_2$ are highly anisotropic, with particularly heavy electron effective masses in the k_z direction but much lighter electrons in the k_x direction.

The very light electron effective masses in the k_x direction result from the highly connected face-sharing Bi^{3+} polyhedra

https://doi.org/10.1021/acs.chemmater.4c00188
Chem. Mater. 2024, 36, 4530–4541

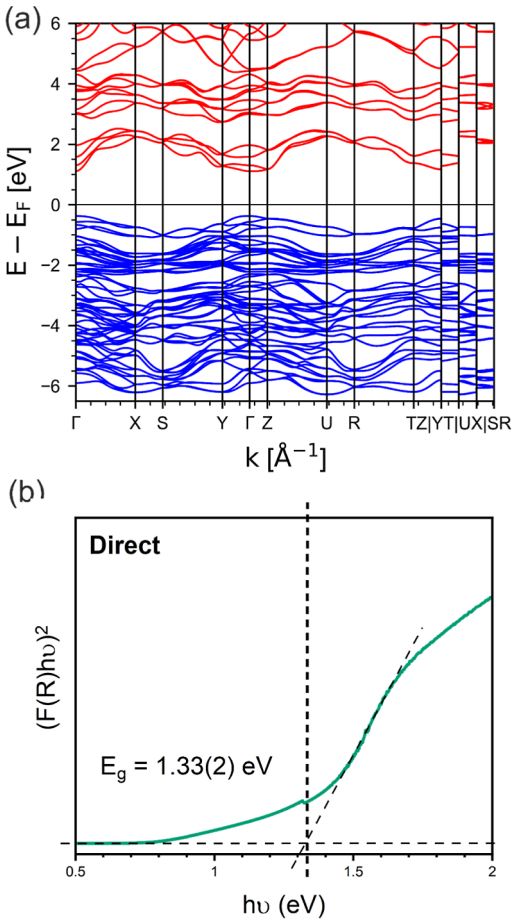

Figure 4. (a) Band structure of $CuBiSeCl_2$ calculated using the HSE06 functional with SOC contributions. Valence band electronic states are shown in blue and the conduction band electronic states in red. (b) Tauc plot derived from UV−vis spectrometry measurements. The direct band gap for $CuBiSeCl_2$ is extrapolated using the Tauc plot and determined to be 1.33(2) eV.

Table 1. Electron (m_e*) and Hole (m_h*) Effective Masses (Relative to the Mass of an Electron, m_0) Calculated as Part of This Study from the Band Structures of $CuBiSCl_2$ (*Cmcm*), $CuBiSeCl_2$ (*Cmcm*), and $CuBiSeCl_2$ (*Pnma*) in the k_x, k_y, and k_z Directions

$CuBiSeCl_2$ (*Pnma*)[a]	k_y ($\Gamma \rightarrow Y$)	k_z ($\Gamma \rightarrow Z$)	k_x ($\Gamma \rightarrow X$)
m_e* (m_0)	1.0	12	0.2
m_h* (m_0)	8	1.6	4
$CuBiSeCl_2$ (*Cmcm*)	k_x ($Y \rightarrow X1$)	k_y ($Y \rightarrow \Gamma$)	k_z ($Y \rightarrow T$)
m_e* (m_0)	3	4.2	0.7
m_h* (m_0)	2.5	0.7	1.3
$CuBiSCl_2$ (*Cmcm*)			
m_e* (m_0)	0.25	3	0.65
m_h* (m_0)	2.9	0.75	1.1

[a]Indicates that the effective masses for the *Pnma* structure of $CuBiSeCl_2$ have been reordered relative to the *Cmcm* structures such that the directions are related by $k_x \rightarrow k_z$, $k_z \rightarrow k_y$, and $k_y \rightarrow k_x$ to account for symmetry lowering effects between *Cmcm* and *Pnma* and allow for ease of comparison between different symmetries.

and corner-sharing Cu^+ octahedra, creating "channels" for the charge carriers. These channels are visible in Figure 1a,d. In a similar way, the moderate effective masses in the k_y direction result from the edge-sharing Cu^+ octahedra and face-sharing Bi^{3+} polyhedra, providing pathways for conductivity. Electrons are more mobile than holes in both the k_x and k_y directions.

The heavy electrons in the k_z direction may be a result of the displacement of Cu^+ away from the octahedral center, with the reduced orbital overlap between Cu^+ and Cl^- weakening the pathway for charge carriers and therefore reducing the conductivity through the network. Therefore, these anisotropic effective masses are likely to result from the anisotropic bonding in $CuBiSeCl_2$ that arises due to the inclusion of mixed anions in the structure.

The calculated effective masses for all compounds are anisotropic, suggesting that this is characteristic of the structure of these materials. $CuBiSCl_2$ (*Cmcm*) exhibits light effective masses along k_x (0.25 m_0) and k_z (0.65 m_0), with electrons being more mobile than holes in both directions. Substituting S for Se into the same *Cmcm* structure has the effect of increasing the electron effective masses observed along k_x (3 m_0), with holes now being more mobile than electrons in this direction. The electron effective mass in the k_z direction also increases slightly (0.7 m_0). Increases in the calculated effective masses observed going from the sulfide to the selenide *Cmcm* structures probably arise due to longer bond distances, which reduce the orbital overlap between atomic species.

Interestingly, when comparing with the calculated effective masses for the experimentally observed *Pnma* structure of $CuBiSeCl_2$, it is found that m_e in the k_z direction of $CuBiSCl_2$ decreases to 0.2 m_0 in the corresponding k_x direction in *Pnma* $CuBiSeCl_2$. Likewise, m_e along k_x also decreases from 3 to 1 m_0 in the corresponding k_y direction between the *Cmcm* and *Pnma* structures of $CuBiSeCl_2$, respectively.

The reduction in electron effective masses in the k_x and k_z directions between hypothetical $CuBiSeCl_2$ (*Cmcm*) and experimentally observed $CuBiSeCl_2$ (*Pnma*) corresponds to the Cu^+ displacement, which occurs in the a−c plane. In particular, the electron effective mass in the c direction is substantially reduced as a result of the significant Cu^+ displacement toward the octahedral edge in this direction, which affords increased orbital overlap within the structure. Consequently, the Cu^+ displacement also has the effect of increasing m_e in the k_y direction in $CuBiSeCl_2$ (*Pnma*) to 12 m_0, which is a sharp increase compared to the analogous direction in $CuBiSCl_2$ (*Cmcm*) (3 m_0).

Though $CuBiSeCl_2$ possesses heavy charge carriers in the k_z direction, this should not be a barrier to its implementation as a thin film for optical absorbing applications, provided it is grown in the correct orientation. For example, Sb_2Se_3 is a well-established solar cell absorber that also exhibits highly anisotropic effective masses.[41] These anisotropic properties are overcome by orienting crystal growth perpendicular to the substrate, allowing for efficient transport along one axis.[42] Saparov et al. also report a method to deposit preferentially oriented thin films,[43] and depositing a axis-aligned $CuBiSeCl_2$ could reduce the effects of the heavy charge carriers along the c axis on the material conductivity.

$CuBiSeCl_2$ may be particularly suited to the deposition of orientated thin films as a result of the effects of the preferred orientation. Analysis of PXRD data measured on $CuBiSeCl_2$ powder and pellets in reflection geometry reveals that $CuBiSeCl_2$ particles preferentially orient in the [h00] and [00l] directions (S24) such that the [0k0] direction is oriented parallel to the surface normal direction, supported by refining the March−Dollase parameters using the Rietveld method.

https://doi.org/10.1021/acs.chemmater.4c00188
Chem. Mater. 2024, 36, 4530−4541

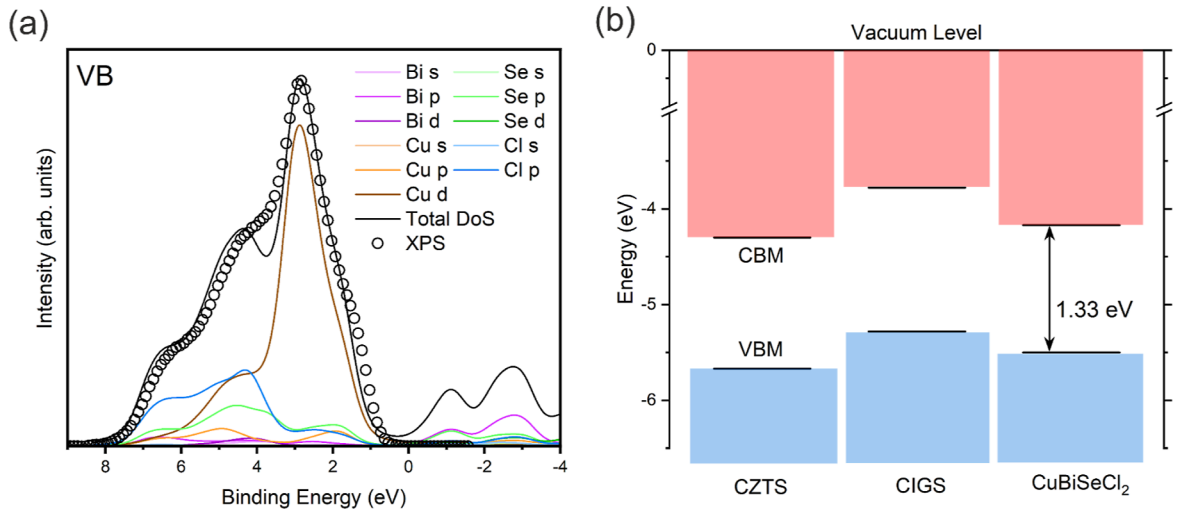

Figure 5. (a) $CuBiSeCl_2$ valence band DoS, calculated using the HSE06 functional with additional SOC contributions and broadened to account for realistic photoemission processes, plotted with valence band XPS data experimentally measured on $CuBiSeCl_2$ powder. (b) Band alignments of $CuBiSeCl_2$ in comparison with optical absorbers with similar chemistries, CZTS and CIGS. The conduction band and valence band states are colored red and blue, respectively.

Diffuse reflectance UV−vis spectrometry was measured on $CuBiSeCl_2$ powder to ascertain the optical band gap. The band gap was determined from a Tauc plot, as shown in Figure 4b, and is found to be 1.33(2) eV, in good agreement with the value derived from the band structure calculations (1.5 eV). Complete agreement between the experiment and calculations is not expected since the DFT calculates the band structure at 0 K, whereas UV−vis diffuse reflectance was measured at 300 K. However, as the temperature is increased, the calculated band gap will decrease, indicating even better agreement between calculation and experiment. $CuBiSeCl_2$ is measured to have a lower band gap than $CuBiSCl_2$, with the value increasing from 1.33(2) to 1.44 eV between the two compounds, respectively. A reduction in band gap with increasing Se content is observed in materials with related chemistries, including $CuSb(S_xSe_{1-x})_2$,[44] $BiCuS_xSe_{1-x}O$,[45] and $BaCu_2Sn(Se_xS_{1-x})_4$.[46]

A long sub-bandgap absorption (Urbach) edge is present in the Tauc plot of $CuBiSeCl_2$, indicative of either structural (static) or thermal (dynamic) disorder present in the material.[47] More specifically, the size of this Urbach edge is directly influenced by lattice vibrations in the material,[48] and in LHPs, it has been shown that increased electron−phonon scattering enlarges the Urbach edge.[49] Modeling of heat capacity data from $CuBiSeCl_2$ (see Section 3.2) confirms the presence of several localized phonon modes, suggesting that a complex landscape of lattice vibrations in the material influence band edge disorder, resulting in the extended Urbach edge.

To understand the electronic structure of $CuBiSeCl_2$ in more detail, experimental measurement of the valence band using XPS was combined with partial density of states (pDoS) calculations. Figure 5a shows valence band XPS compared to pDoS that has been corrected to account for realistic photoemission processes, including lifetime broadening and spectrometer resolution. The broadening processes used are discussed in greater detail in the Supporting Information (S29 and S30).

The corrected pDoS indicates that Cu 3d states dominate the top of the valence band, while Cl 3p states occupy higher binding energies much deeper into the valence band. Se 4p, Cu 3p, and, to a lesser extent, Bi 5p/5d states cover a broad range of binding energies between 0 and 6 eV in the valence band. There is some hybridization between the Cu 3d, Se 4p, and Cl 3p states at higher binding energy in the valence band, likely due to the overlap of Cu, Se, and Cl orbitals in the tetrahedral $CuSe_2Cl_2$ bonding environment. Similarly, hybridization between Bi 5p and Se 4p/Cl 3p states at the bottom of the conduction band may arise from the Bi−Se/Bi−Cl bonding in the Bi polyhedra.

A sharp peak arising from Cu orbital contributions is also observed in the pDoS of similar chalcogenide and chalcohalide materials, including Cu_3BiS_3 ($P2_12_12_1$)[50] and Bi_2CuSe_3I ($C2/m$),[51] in which Cu occupies different bonding environments. This suggests that Cu has a commanding effect on both chalcogen and halogen orbitals across different structures with similar chemistries, heavily influencing the top of the valence band. Comparisons between the pDoS of $CuBiSCl_2$ and $CuBiSeCl_2$ reveal that the valence band consists of a hybridization of Cu 3d, Ch 3p (where Ch = S, Se), and Cl 4p states in both materials, though the number of Se 3p states in the $CuBiSeCl_2$ valence band is lower than the number of S 3p states in the $CuBiSCl_2$ valence band. This is attributed to the reduced orbital overlap in $CuBiSeCl_2$ as a result of longer bond distances.

Excellent agreement is observed between the XPS data and pDoS, suggesting that the DFT calculations provide accurate insights into the electronic character of the material. To enable the development of thin films and prototype devices based on $CuBiSeCl_2$, it is essential to understand the band alignments of the material to allow the selection of suitable device structures and n-type window layers. Figure 5b depicts the band alignments for $CuBiSeCl_2$ alongside well-established semiconductors with similar chemistries, Cu_2ZnSnS_4 (CZTS)[52] and $CuIn_xGa_{1-x}Se_2$ (CIGS).[53] By collecting the SEC region using very low-power XPS, it was possible to determine the IP and the valence band minimum (full description in the Supporting Information S32−S34). The CBM could then be located using the band gap, determined from diffuse reflectance UV−vis Spectroscopy, and found to be 1.33(2)

https://doi.org/10.1021/acs.chemmater.4c00188
Chem. Mater. 2024, 36, 4530−4541

eV, in good agreement with computational predictions. CdS has already been demonstrated as a successful window layer for CZTS and CIGS[54,55] and, given the comparable band alignments, could also find application as a suitable window layer for devices based on $CuBiSeCl_2$.

The environmental stability of $CuBiSeCl_2$ was characterized to understand the powder degradation over time with exposure to air and moisture. $CuBiSeCl_2$ powder was found to be stable in ambient air for over 1 month (S35). Analysis of PXRD data measured at regular time intervals shows that there is no change in the data taken after 10 min and 3 weeks of air exposure. However, after 9 weeks in ambient conditions, broad peaks consistent with the formation of BiOCl become visible. After mixing with water, depositing onto a glass slide, and drying for 24 h, it was observed that the black powder underwent a slight color change to pink around the very edges. A comparison of PXRD data from before and after water exposure reveals the appearance of small impurity peaks, consistent with the formation of BiOCl (S36).

3.1. Electronic Properties. The electronic resistivity and Seebeck coefficient were measured on a dense pellet (~88%) of $CuBiSeCl_2$, parallel to the pressing direction, between 2 and 300 K (Figure 6) to understand the electronic transport within the material. The pellet was highly textured, as described above, with a preferential orientation in both the *a* and *c* directions (S24). Below 250 K, the resistance of $CuBiSeCl_2$ became too high for any meaningful resistivity or Seebeck coefficient data to be collected; hence, these properties are only shown at approximately 250 K.

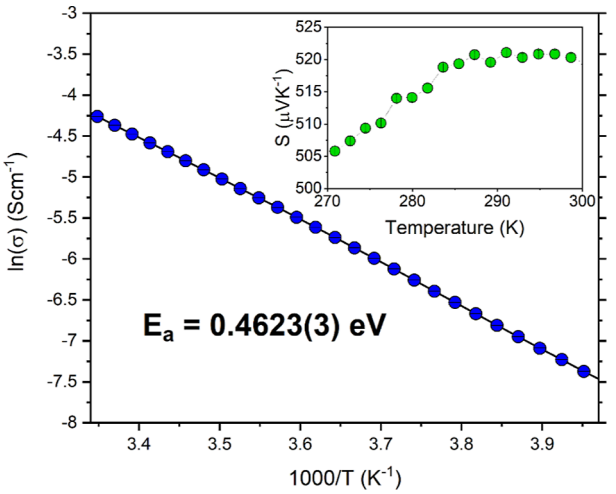

Figure 6. Arrhenius plot calculated from measuring the resistivity of $CuBiSeCl_2$ parallel to the pressing direction between 250 and 300 K, with Seebeck coefficient measurement between 270 and 300 K inset. The activation energy is determined to be 0.4623(3) eV.

At 300 K, $CuBiSeCl_2$ is measured to have a large, positive Seebeck coefficient of 519.0(6) μVK^{-1}, confirming that the material is a p-type semiconductor.

The electronic resistivity of $CuBiSeCl_2$ exhibits behavior typical of a semiconductor, and a large resistivity of ~6376(3) Ωm is measured at 300 K, consistent with the prediction of heavy charge carriers. Using the Arrhenius equation and by plotting $\ln(\sigma)$, where σ is the electronic conductivity, as a function of $1000/T$, the activation energy (E_a) could be extracted from the gradient and was found to be 0.4623(3) eV.

For an intrinsic semiconductor, it is expected that E_a is half the band gap, which in this case would be equal to 0.65 eV. We attribute the lower observed E_a to the p-type conductivity of $CuBiSeCl_2$, which results in an additional extrinsic charge carrier density. It is likely that the measured E_a corresponds to the ionization energy of an acceptor level positioned above the valence band, an effect that has been observed in other p-type semiconductors. For example, p-type $CuAlO_2$ possesses a direct band gap of 3.47 eV and a 0.7 eV activation energy.[56] Similarly, Ga_2O_3 exhibits an ultrawide 4.8 eV band gap, which is almost four times the E_a (1.24 eV).[57] In both cases, the discrepancy between the band gap and activation energy is associated with the presence of an acceptor level above the valence band.

3.2. Thermal Properties. Along with the resistivity and Seebeck coefficient, the thermal conductivity was simultaneously measured on the same dense pellet of $CuBiSeCl_2$, parallel to the pressing direction, between 2 and 300 K (Figure 7a). The behavior of the thermal conductivity of $CuBiSeCl_2$ between 2 and 300 K is consistent with that of a crystalline material in which heat is transported by propagating phonons. At low temperatures, the thermal conductivity increases rapidly and peaks at 0.646(1) W K^{-1} m^{-1} at ~35 K before decreasing to 0.27(4) W K^{-1} m^{-1} at 225 K, where it plateaus and is almost temperature-independent up to 300 K. Observation of the peak at ~35 K in κ confirms the phonon-crystal characteristics of $CuBiSeCl_2$.

The heat capacity of $CuBiSeCl_2$ was measured on a fragment of the same dense pellet to provide insights into the behavior of phonons within the material and the origin of the particularly low thermal conductivity (Figure 7b,c). The data were modeled using a combination of linear, Debye, and Einstein terms, the parameters of which are summarized in Table 2.

The observation of an excess of specific heat at low temperatures, which often arises from highly localized vibrations,[58] is accurately modeled using 2 Einstein temperatures, in addition to a linear term. This indicates the presence of several highly localized phonon modes within the structure.[59] The Debye temperatures obtained from the heat capacity modeling enable the associated speeds of sound in $CuBiSeCl_2$ to be calculated, which can provide information on the low thermal conductivity in the material. Further detail on the modeling used in this study may be found in Supplementary Information S37.

Using these values, the minimum thermal conductivity under the assumptions of the Cahill model (κ_{min}) for $CuBiSeCl_2$ was calculated (shown by the dashed line in Figure 7a).[60] Unusually, the calculated minimum thermal conductivity (0.40 W K^{-1} m^{-1}) is greater than the measured data (0.27 (4) W K^{-1} m^{-1}) at 300 K. However, a diffuson model (κ_{diff}) of the thermal conductivity, which includes the experimentally determined θ_{D1}, θ_{D2}, θ_{E1}, θ_{E2}, and v_s, accurately captures the high temperature behavior of the measured data (shown in Figure 7a in red).[61] This indicates that the thermal conductivity of the material must likely be understood through a two-channel model, where propagons dominate at low temperatures (resulting in the peak at 35 K), while diffusons dominate at higher temperatures (resulting in the plateau in thermal conductivity above 225 K).[62] This effect has previously been observed in Ag_9GaSe_6 and was attributed to small interband spacings between phonon modes.[63]

https://doi.org/10.1021/acs.chemmater.4c00188
Chem. Mater. 2024, 36, 4530−4541

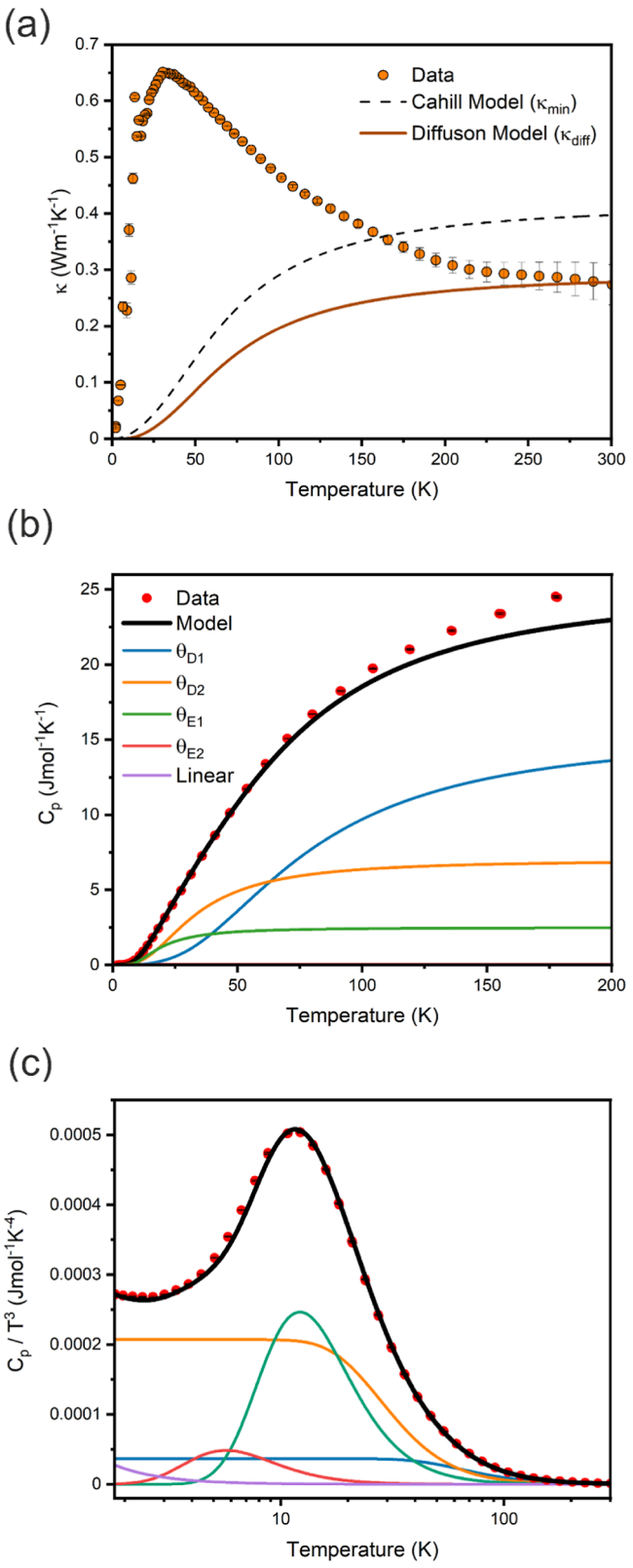

Figure 7. (a) Thermal conductivity of $CuBiSeCl_2$ measured parallel to the pressing direction shown with Cahill (κ_{min}) and diffuson-based (κ_{diff}) models; fitted heat capacity data of $CuBiSeCl_2$ shown as (b) C_p and (c) C_p/T^3 with Debye, Einstein, and linear components shown.

The origin of the low thermal conductivity in $CuBiSeCl_2$ can be understood by considering the structure and bonding present in the material. Achieving bonding anisotropy and structural anharmonicity are key design criteria for novel materials with ultralow thermal conductivities,[64,65] as reducing or disrupting the bonding between species reduces the speed of sound and, therefore, the transport of heat through a material. The need for multiple Debye terms to accurately model the observed heat capacity can arise from the contributions of species with distinct bonds or masses within the structure. The higher-frequency represented by θ_{D1} (320 K) is associated with the more ionic character of Cu−Se/Cl bonds and the lower mass of Cu, while the lower frequency contributions of θ_{D2} (138 K) arise from the increased mass and more covalent bonding of Bi and can be understood when considering the local $CuSe_2Cl_2$ and $BiSe_2Cl_6$ environments within $CuBiSeCl_2$. Certainly, the room temperature phonon mean free paths calculated from these Debye temperatures are of the order of 2−3 Å (S38 and S39), comparable to the interatomic distances within $CuBiSeCl_2$, which indicates strong suppression of phonon propagation throughout the structure. In addition, 2 Einstein temperatures of θ_{E1} = 60 K and θ_{E2} = 28 K are required to model the excess specific heat evident from the experimentally measured heat capacity, the contributions of which represent those of localized oscillators with singular vibrational frequencies and thus nonpropagating modes. Again, the heavier mass of Bi is associated with a lower frequency θ_{E2} term. The higher-frequency Einstein temperature of θ_{E1} can be attributed to the local environment of Cu. As described above, Cu displaces from the center of an octahedral environment, observed in $CuBiSCl_2$, to yield a tetrahedral $CuSe_2Cl_2$ environment in $CuBiSeCl_2$. We note that the isotropic displacement parameter U_{iso} for the Cu site [0.01027(6) Å^2] in the single crystal structure of $CuBiSeCl_2$ solved at 100 K is approximately double that of any other species in the structure (Table S16). This difference in U_{iso} values for each site is significantly increased at room temperature from refinement of the model against PXRD data (Table S20), where the U_{iso} for Cu is 0.044(2) Å^2, and the next largest is that of the Cl2 site [U_{iso} = 0.014(3) Å^2]. Large U_{iso} values can be indicative of weak restoring forces and consequently weak bonding and anharmonicity.[66,67] This indicates that Cu is loosely bound in the structure of $CuBiSeCl_2$, despite the displacement to achieve higher bond valence. It is well established that loosely bound atoms can disrupt the propagating vibrational modes within the surrounding structural framework and are commonplace in materials such as clathrates and skutterudites;[68−71] hence, Cu acts as a localized oscillator attributed to θ_{E1} and significantly enhances phonon scattering within the structure of $CuBiSeCl_2$. The combination of multiple anions, and therefore bonding environments in $CuBiSeCl_2$, infers a complex phonon landscape with localized vibrations that result in low speeds of sound and a low κ that is comparable to many other inorganic materials that exhibit low thermal conductivity.

Table 2. Heat Capacity Parameters Determined from Modeling Heat Capacity Measurements for $CuBiSeCl_2$

compound	θ_{D1} (K)	θ_{D2} (K)	θ_{E1} (K)	θ_{E2} (K)	γ (J mol^{-1} K^{-2})
$CuBiSeCl_2$	320	138	60	28	0.00009

For example, a similar effect is observed in the structurally complex $Cu_4Bi_4Ch_9$ (Ch = S, Se) materials, whereby substitution of S for Se increases the volume of the coordination environment and reduces the localization of the Cu atoms.[72] This increases the lattice anharmonicity in the

https://doi.org/10.1021/acs.chemmater.4c00188
Chem. Mater. 2024, 36, 4530−4541

selenide material, increasing the frequency of phonon scattering events, which manifests itself as a reduction in room temperature κ between $Cu_4Bi_4S_9$ (0.44 K^{-1} m^{-1}) and $Cu_4Bi_4Se_9$ (0.29 W K^{-1} m^{-1}). The similarity in κ between $CuBiSeCl_2$ and $Cu_4Bi_4Se_9$ points to the fact that increased Cu delocalization and the associated phonon scattering are contributing factors to the low thermal conductivity of $CuBiSeCl_2$.

The thermal conductivity of $CuBiSeCl_2$ is also comparable with that observed in other mixed anion materials, including 2D layered materials such as $Bi_4O_4SeCl_2$. Gibson et al. employed the effect of bond anisotropy at the interfaces between layers of BiOCl and Bi_2O_2Se to achieve a material with ultralow thermal conductivity (0.1 W K^{-1} m^{-1}) by minimizing the contribution of longitudinal and transverse phonons to heat transport.[64] $Bi_4O_4Cu_{1.7}Se_{2.7}Cl_{0.3}$, a system based on the intergrowth of Bi_2O_2Se and BiCuSeO layers, also realizes a low thermal conductivity [0.4(1) W K^{-1} m^{-1}] through additional structural complexity.[2]

$CuBiSeCl_2$ is an example of how anionic substitution can introduce structural anharmonicity, modifying the phonon landscape to drive the reduction of heat transport through the material.

4. CONCLUSIONS

We have reported the synthesis, crystal structure, and properties of $CuBiSeCl_2$, a previously unreported p-type chalcohalide semiconductor with low thermal conductivity and a suitable band gap for solar-absorbing applications. Cationic displacements that arise from heterogeneous bonding induced by the different anions result in anisotropic charge carrier transport, with light effective masses observed in the *a* direction. As such, for the development of this material as a thin film for application as a potential solar absorber, the *a* axis-oriented deposition is suggested to utilize the superior effective masses along this direction. The low thermal conductivity observed in $CuBiSeCl_2$ demonstrates how the combination of multiple anions can lead to separate structural motifs that significantly reduce κ, as evidenced through experimental heat capacity and structural refinement through loosely bound Cu species and bonding anharmonicity. As such, $CuBiSeCl_2$ is an example of the opportunities for property modification through the application of mixed anion chemistry, as shown by the variations in the structural, electronic, and physical properties of $CuBiSeCl_2$ relative to known materials with similar structures.

■ ASSOCIATED CONTENT

Data Availability Statement

The data underlying this study are openly available in University of Liverpool Data Repository at https://doi.org/10.17638/datacat.liverpool.ac.uk/2550.

Supporting Information

The Supporting Information is available free of charge at https://pubs.acs.org/doi/10.1021/acs.chemmater.4c00188.

Crystal structure details and comparisons; compositional analysis; TEM imaging; computational details and band structures; fitted core level XPS spectra; XPS survey spectra; environmental stability PXRDs; and description of thermal property modeling (PDF)

Crystallographic data for $CuBiSeCl_2$ (CIF)

■ AUTHOR INFORMATION

Corresponding Author

Matthew J. Rosseinsky − *Department of Chemistry, Materials Innovation Factory, University of Liverpool, Liverpool L7 3NY, U.K.*; orcid.org/0000-0002-1910-2483; Email: m.j.rosseinsky@liverpool.ac.uk

Authors

Cara J. Hawkins − *Department of Chemistry, Materials Innovation Factory, University of Liverpool, Liverpool L7 3NY, U.K.*

Jon A. Newnham − *Department of Chemistry, Materials Innovation Factory, University of Liverpool, Liverpool L7 3NY, U.K.*; orcid.org/0000-0002-8408-7232

Batoul Almoussawi − *Department of Chemistry, Materials Innovation Factory, University of Liverpool, Liverpool L7 3NY, U.K.*

Nataliya L. Gulay − *Department of Chemistry, Materials Innovation Factory, University of Liverpool, Liverpool L7 3NY, U.K.*; orcid.org/0000-0002-8005-4855

Samuel L. Goodwin − *Department of Chemistry, Materials Innovation Factory, University of Liverpool, Liverpool L7 3NY, U.K.*

Marco Zanella − *Department of Chemistry, Materials Innovation Factory, University of Liverpool, Liverpool L7 3NY, U.K.*

Troy D. Manning − *Department of Chemistry, Materials Innovation Factory, University of Liverpool, Liverpool L7 3NY, U.K.*; orcid.org/0000-0002-7624-4306

Luke M. Daniels − *Department of Chemistry, Materials Innovation Factory, University of Liverpool, Liverpool L7 3NY, U.K.*; orcid.org/0000-0002-7077-6125

Matthew S. Dyer − *Department of Chemistry, Materials Innovation Factory, University of Liverpool, Liverpool L7 3NY, U.K.*; orcid.org/0000-0002-4923-3003

Tim D. Veal − *Stephenson Institute for Renewable Energy and Department of Physics, University of Liverpool, Liverpool L69 7ZF, U.K.*; orcid.org/0000-0002-0610-5626

John B. Claridge − *Department of Chemistry, Materials Innovation Factory, University of Liverpool, Liverpool L7 3NY, U.K.*

Complete contact information is available at: https://pubs.acs.org/10.1021/acs.chemmater.4c00188

Notes

The authors declare no competing financial interest.

■ ACKNOWLEDGMENTS

The authors thank EPSRC for funding the work (EP/V026887 and EP/X038777). The X-ray Photoelectron Spectroscopy (XPS) data collection was performed at the EPSRC National Facility for XPS ("HarwellXPS"), operated by Cardiff University and UCL, under contract no. PR16195. We thank Diamond Light Source for access to beamline I-19 (proposal CY30461). This work used the ARCHER2 UK National Supercomputing Service (https://www.archer2.ac.uk).

■ REFERENCES

(1) Kageyama, H.; Hayashi, K.; Maeda, K.; Attfield, J. P.; Hiroi, Z.; Rondinelli, J. M.; Poeppelmeier, K. R. Expanding frontiers in materials chemistry and physics with multiple anions. *Nat. Commun.* **2018**, *9*, 772.

(2) Gibson, Q. D.; Dyer, M. S.; Whitehead, G. F. S.; Alaria, J.; Pitcher, M. J.; Edwards, H. J.; Claridge, J. B.; Zanella, M.; Dawson, K.; Manning, T. D.; Dhanak, V. R.; Rosseinsky, M. J. $Bi_4O_4Cu_{1.7}Se_{2.7}Cl_{0.3}$: Intergrowth of BiOCuSe and Bi_2O_2Se Stabilized by the Addition of a Third Anion. *J. Am. Chem. Soc.* **2017**, *139* (44), 15568−15571.
(3) Yan, M.; Tang, R.-L.; Zhou, W.; Liu, W.; Guo, S.-P. Pb_3SBrI_3: the first Pb-based chalcohalide with multiple halogens features a unique two-dimensional structure composed of diverse Pb-centered polyhedra. *Dalton Trans.* **2022**, *51* (34), 12921−12927.
(4) Chen, X.; Jing, Q.; Ok, K. M. $Pb_{18}O_8Cl_{15}I_5$: A Polar Lead Mixed Oxyhalide with Unprecedented Architecture and Excellent Infrared Nonlinear Optical Properties. *Angew. Chem., Int. Ed.* **2020**, *59* (46), 20323−20327.
(5) Tsujimoto, Y.; Sathish, C. I.; Hong, K.-P.; Oka, K.; Azuma, M.; Guo, Y.; Matsushita, Y.; Yamaura, K.; Takayama-Muromachi, E. Crystal Structural, Magnetic, and Transport Properties of Layered Cobalt Oxyfluorides, $Sr_2CoO_{3+x}F_{1-x}$ ($0 \leq x \leq 0.15$). *Inorg. Chem.* **2012**, *51* (8), 4802−4809.
(6) Kamihara, Y.; Hiramatsu, H.; Hirano, M.; Kawamura, R.; Yanagi, H.; Kamiya, T.; Hosono, H. Iron-Based Layered Superconductor: LaOFeP. *J. Am. Chem. Soc.* **2006**, *128* (31), 10012−10013.
(7) Wu, H.; Erbing, A.; Johansson, M. B.; Wang, J.; Kamal, C.; Odelius, M.; Johansson, E. M. J. Mixed-Halide Double Perovskite Cs_2AgBiX_6 (X = Br, I) with Tunable Optical Properties via Anion Exchange. *ChemSusChem* **2021**, *14* (20), 4507−4515.
(8) Hodges, J. M.; Xia, Y.; Malliakas, C. D.; Slade, T. J.; Wolverton, C.; Kanatzidis, M. G. Mixed-Valent Copper Chalcogenides: Tuning Structures and Electronic Properties Using Multiple Anions. *Chem. Mater.* **2020**, *32* (23), 10146−10154.
(9) Kim, S.-W.; Pereira, N.; Chernova, N. A.; Omenya, F.; Gao, P.; Whittingham, M. S.; Amatucci, G. G.; Su, D.; Wang, F. Structure Stabilization by Mixed Anions in Oxyfluoride Cathodes for High-Energy Lithium Batteries. *ACS Nano* **2015**, *9* (10), 10076−10084.
(10) Yao, W.; Sougrati, M.-T.; Hoang, K.; Hui, J.; Lightfoot, P.; Armstrong, A. R. $Na_2Fe(C_2O_4)F_2$: A New Iron-Based Polyoxyanion Cathode for Li/Na Ion Batteries. *Chem. Mater.* **2017**, *29* (5), 2167−2172.
(11) Tang, W. S.; Yoshida, K.; Soloninin, A. V.; Skoryunov, R. V.; Babanova, O. A.; Skripov, A. V.; Dimitrievska, M.; Stavila, V.; Orimo, S.-I.; Udovic, T. J. Stabilizing Superionic-Conducting Structures via Mixed-Anion Solid Solutions of Monocarba-*closo*-borate Salts. *ACS Energy Lett.* **2016**, *1* (4), 659−664.
(12) Sato, N.; Kuroda, N.; Nakamura, S.; Katsura, Y.; Kanazawa, I.; Kimura, K.; Mori, T. Bonding heterogeneity in mixed-anion compounds realizes ultralow lattice thermal conductivity. *J. Mater. Chem. A* **2021**, *9* (39), 22660−22669.
(13) Li, F.; Li, J.-F.; Zhao, L.-D.; Xiang, K.; Liu, Y.; Zhang, B.-P.; Lin, Y.-H.; Nan, C.-W.; Zhu, H.-M. Polycrystalline BiCuSeO oxide as a potential thermoelectric material. *Energy Environ. Sci.* **2012**, *5* (5), 7188.
(14) Pei, Y.-L.; He, J.; Li, J.-F.; Li, F.; Liu, Q.; Pan, W.; Barreteau, C.; Berardan, D.; Dragoe, N.; Zhao, L.-D. High thermoelectric performance of oxyselenides: intrinsically low thermal conductivity of Ca-doped BiCuSeO. *NPG Asia Mater.* **2013**, *5* (5), No. e47.
(15) Ran, M.-Y.; Zhou, S.-H.; Wei, W.; Song, B.-J.; Shi, Y.-F.; Wu, X.-T.; Lin, H.; Zhu, Q.-L. Quaternary Chalcohalides $CdSnSX_2$ (X = Cl or Br) with Neutral Layers: Syntheses, Structures, and Photocatalytic Properties. *Inorg. Chem.* **2021**, *60* (5), 3431−3438.
(16) Johnsen, S.; Liu, Z.; Peters, J. A.; Song, J.-H.; Nguyen, S.; Malliakas, C. D.; Jin, H.; Freeman, A. J.; Wessels, B. W.; Kanatzidis, M. G. Thallium Chalcohalides for X-ray and γ-ray Detection. *J. Am. Chem. Soc.* **2011**, *133* (26), 10030−10033.
(17) Sun, Y.-Y.; Shi, J.; Lian, J.; Gao, W.; Agiorgousis, M. L.; Zhang, P.; Zhang, S. Discovering lead-free perovskite solar materials with a split-anion approach. *Nanoscale* **2016**, *8* (12), 6284−6289.
(18) Perera, S.; Hui, H.; Zhao, C.; Xue, H.; Sun, F.; Deng, C.; Gross, N.; Milleville, C.; Xu, X.; Watson, D. F.; Weinstein, B.; Sun, Y. Y.; Zhang, S.; Zeng, H. Chalcogenide perovskites - an emerging class of ionic semiconductors. *Nano Energy* **2016**, *22*, 129−135.
(19) Gupta, T.; Ghoshal, D.; Yoshimura, A.; Basu, S.; Chow, P. K.; Lakhnot, A. S.; Pandey, J.; Warrender, J. M.; Efstathiadis, H.; Soni, A.; Osei-Agyemang, E.; Balasubramanian, G.; Zhang, S.; Shi, S. F.; Lu, T. M.; Meunier, V.; Koratkar, N. An Environmentally Stable and Lead-Free Chalcogenide Perovskite. *Adv. Funct. Mater.* **2020**, *30* (23), 2001387.
(20) Palazon, F. Metal Chalcohalides: Next Generation Photovoltaic Materials? *Sol. RRL* **2022**, *6* (2), 2100829.
(21) Nie, R.; Lee, K. S.; Hu, M.; Paik, M. J.; Seok, S. I. Heteroleptic Tin-Antimony Sulfoiodide for Stable and Lead-free Solar Cells. *Matter* **2020**, *3* (5), 1701−1713.
(22) Nicolson, A.; Breternitz, J.; Kavanagh, S. R.; Tomm, Y.; Morita, K.; Squires, A. G.; Tovar, M.; Walsh, A.; Schorr, S.; Scanlon, D. O. Interplay of Static and Dynamic Disorder in the Mixed-Metal Chalcohalide $Sn_2SbS_2I_3$. *J. Am. Chem. Soc.* **2023**, *145* (23), 12509−12517.
(23) Ming, C.; Chen, Z.; Zhang, F.; Gong, S.; Wu, X.; Jiang, J.; Ye, T.; Xu, Q.; Yang, K.; Wang, L.; Cao, X.; Yang, S.; Zhang, S.; Zhang, Y.; Shi, J.; Sun, Y. Y. Mixed Chalcogenide-Halides for Stable, Lead-Free and Defect-Tolerant Photovoltaics: Computational Screening and Experimental Validation of $CuBiSCl_2$ with Ideal Band Gap. *Adv. Funct. Mater.* **2022**, *32*, 32.
(24) Coelho, A. A. Whole-profile structure solution from powder diffraction data using simulated annealing. *J. Appl. Crystallogr.* **2000**, *33* (3), 899−908.
(25) Stephens, P. W. Phenomenological model of anisotropic peak broadening in powder diffraction. *J. Appl. Crystallogr.* **1999**, *32* (2), 281−289.
(26) Nowell, H.; Barnett, S. A.; Christensen, K. E.; Teat, S. J.; Allan, D. R. I19, the small-molecule single-crystal diffraction beamline at Diamond Light Source. *J. Synchrotron Radiat.* **2012**, *19* (3), 435−441.
(27) Winter, G. *xia2*: an expert system for macromolecular crystallography data reduction. *J. Appl. Crystallogr.* **2010**, *43* (1), 186−190.
(28) Winter, G.; Waterman, D. G.; Parkhurst, J. M.; Brewster, A. S.; Gildea, R. J.; Gerstel, M.; Fuentes-Montero, L.; Vollmar, M.; Michels-Clark, T.; Young, I. D.; Sauter, N. K.; Evans, G. *DIALS*: implementation and evaluation of a new integration package. *Acta Crystallogr., Sect. D: Struct. Biol.* **2018**, *74* (2), 85−97.
(29) Sheldrick, G. M. A short history of *SHELX*. *Acta Crystallogr., Sect. A: Found. Crystallogr.* **2008**, *64* (1), 112−122.
(30) Dolomanov, O. V.; Bourhis, L. J.; Gildea, R. J.; Howard, J. A. K.; Puschmann, H. *OLEX2*: a complete structure solution, refinement and analysis program. *J. Appl. Crystallogr.* **2009**, *42* (2), 339−341.
(31) Makuła, P.; Pacia, M.; Macyk, W. How To Correctly Determine the Band Gap Energy of Modified Semiconductor Photocatalysts Based on UV−Vis Spectra. *J. Phys. Chem. Lett.* **2018**, *9* (23), 6814−6817.
(32) Kresse, G.; Furthmüller, J. Efficient iterative schemes for *ab initio* total-energy calculations using a plane-wave basis set. *Phys. Rev. B: Condens. Matter Mater. Phys.* **1996**, *54* (16), 11169−11186.
(33) Kresse, G.; Joubert, D. From ultrasoft pseudopotentials to the projector augmented-wave method. *Phys. Rev. B: Condens. Matter Mater. Phys.* **1999**, *59* (3), 1758−1775.
(34) Krukau, A. V.; Vydrov, O. A.; Izmaylov, A. F.; Scuseria, G. E. Influence of the exchange screening parameter on the performance of screened hybrid functionals. *J. Chem. Phys.* **2006**, *125* (22), 224106.
(35) Steiner, S.; Khmelevskyi, S.; Marsmann, M.; Kresse, G. Calculation of the magnetic anisotropy with projected-augmented-wave methodology and the case study of disordered $Fe_{1-x}Co_x$. *Phys. Rev. B* **2016**, *93* (22), 224425.
(36) Setyawan, W.; Curtarolo, S. High-throughput electronic band structure calculations: Challenges and tools. *Comput. Mater. Sci.* **2010**, *49* (2), 299−312.
(37) Ruck, M.; Poudeu Poudeu, P. F.; Söhnel, T. Synthese, Kristallstruktur und elektronische Bandstruktur der isotypen Sulfid-chloride $CuBiSCl_2$ und $AgBiSCl_2$. *Z. Anorg. Allg. Chem.* **2004**, *630*, 63−67.

https://doi.org/10.1021/acs.chemmater.4c00188
Chem. Mater. 2024, 36, 4530−4541

(38) Xiao, Z.; Du, K. Z.; Meng, W.; Mitzi, D. B.; Yan, Y. Chemical Origin of the Stability Difference between Copper (I)- and Silver (I)-Based Halide Double Perovskites. *Angew. Chem., Int. Ed.* **2017**, *56* (40), 12107−12111.
(39) Doussier, C.; Moëlo, Y.; Léone, P. Synthesis and crystal structures of four new bromo-chalcogenides: $MnSbS_2Br$, $MnBiSe_2Br$ and two allotropic forms of $MnSbSe_2Br$. Crystal chemistry of the Mn PnQ_2 X family (Pn = Sb, Bi; Q = S, Se; X = Cl, Br, I). *Solid State Sci.* **2006**, *8*, 652−659.
(40) Shannon, R. D. Revised effective ionic radii and systematic studies of interatomic distances in halides and chalcogenides. *Acta Crystallogr., Sect. A: Found. Adv.* **1976**, *32* (5), 751−767.
(41) Wang, X.; Li, Z.; Kavanagh, S. R.; Ganose, A. M.; Walsh, A. Lone pair driven anisotropy in antimony chalcogenide semiconductors. *Phys. Chem. Chem. Phys.* **2022**, *24* (12), 7195−7202.
(42) Zhou, Y.; Wang, L.; Chen, S.; Qin, S.; Liu, X.; Chen, J.; Xue, D.-J.; Luo, M.; Cao, Y.; Cheng, Y.; Sargent, E. H.; Tang, J. Thin-film Sb_2Se_3 photovoltaics with oriented one-dimensional ribbons and benign grain boundaries. *Nat. Photonics* **2015**, *9* (6), 409−415.
(43) Saparov, B.; Hong, F.; Sun, J.-P.; Duan, H.-S.; Meng, W.; Cameron, S.; Hill, I. G.; Yan, Y.; Mitzi, D. B. Thin-Film Preparation and Characterization of $Cs_3Sb_2I_9$: A Lead-Free Layered Perovskite Semiconductor. *Chem. Mater.* **2015**, *27* (16), 5622−5632.
(44) Takei, K.; Maeda, T.; Wada, T. Crystallographic and optical properties of $CuSbS_2$ and $CuSb(S_{1-x}Se_x)_2$ solid solution. *Thin Solid Films* **2015**, *582*, 263−268.
(45) Berardan, D.; Li, J.; Amzallag, E.; Mitra, S.; Sui, J.; Cai, W.; Dragoe, N. Structure and Transport Properties of the BiCuSeO-BiCuSO Solid Solution. *Materials* **2015**, *8* (3), 1043−1058.
(46) Ge, J.; Yu, Y.; Yan, Y. Earth-abundant trigonal $BaCu_2Sn(Se_xS_{1-x})_4$ (x = 0−0.55) thin films with tunable band gaps for solar water splitting. *J. Mater. Chem. A* **2016**, *4* (48), 18885−18891.
(47) Ugur, E.; Ledinský, M.; Allen, T. G.; Holovský, J.; Vlk, A.; De Wolf, S. Life on the Urbach Edge. *J. Phys. Chem. Lett.* **2022**, *13* (33), 7702−7711.
(48) Ledinsky, M.; Schönfeldová, T.; Holovský, J.; Aydin, E.; Hájková, Z.; Landová, L.; Neyková, N.; Fejfar, A.; De Wolf, S. Temperature Dependence of the Urbach Energy in Lead Iodide Perovskites. *J. Phys. Chem. Lett.* **2019**, *10* (6), 1368−1373.
(49) Galvani, B.; Suchet, D.; Delamarre, A.; Bescond, M.; Michelini, F. V.; Lannoo, M.; Guillemoles, J.-F.; Cavassilas, N. Impact of Electron−Phonon Scattering on Optical Properties of $CH_3NH_3PbI_3$ Hybrid Perovskite Material. *ACS Omega* **2019**, *4* (25), 21487−21493.
(50) Whittles, T. J.; Veal, T. D.; Savory, C. N.; Yates, P. J.; Murgatroyd, P. A. E.; Gibbon, J. T.; Birkett, M.; Potter, R. J.; Major, J. D.; Durose, K.; Scanlon, D. O.; Dhanak, V. R. Band Alignments, Band Gap, Core Levels, and Valence Band States in Cu_3BiS_3 for Photovoltaics. *ACS Appl. Mater. Interfaces* **2019**, *11* (30), 27033−27047.
(51) Liang, I. C.; Bilc, D. I.; Manoli, M.; Chang, W. Y.; Lin, W. F.; Kyratsi, T.; Hsu, K. F. Syntheses, crystal Structures and electronic Structures of new metal chalcoiodides Bi_2CuSe_3I and $Bi_6Cu_3S_{10}I$. *J. Solid State Chem.* **2016**, *234*, 1−8.
(52) Burton, L. A.; Walsh, A. Band alignment in SnS thin-film solar cells: Possible origin of the low conversion efficiency. *Appl. Phys. Lett.* **2013**, *102* (13), 132111.
(53) Hinuma, Y.; Oba, F.; Kumagai, Y.; Tanaka, I. Ionization potentials of (112) and (112) facet surfaces of $CuInSe_2$ and $CuGaSe_2$. *Phys. Rev. B: Condens. Matter Mater. Phys.* **2012**, *86* (24), 245433.
(54) Yan, C.; Huang, J.; Sun, K.; Johnston, S.; Zhang, Y.; Sun, H.; Pu, A.; He, M.; Liu, F.; Eder, K.; Yang, L.; Cairney, J. M.; Ekins-Daukes, N. J.; Hameiri, Z.; Stride, J. A.; Chen, S.; Green, M. A.; Hao, X. Cu_2ZnSnS_4 solar cells with over 10% power conversion efficiency enabled by heterojunction heat treatment. *Nat. Energy* **2018**, *3* (9), 764−772.
(55) Cho, K. S.; Jang, J.; Park, J.-H.; Lee, D.-K.; Song, S.; Kim, K.; Eo, Y.-J.; Yun, J. H.; Gwak, J.; Chung, C.-H. Optimal CdS Buffer Thickness to Form High-Quality CdS/Cu(In,Ga)Se_2 Junctions in Solar Cells without Plasma Damage and Shunt Paths. *ACS Omega* **2020**, *5* (37), 23983−23988.
(56) Tate, J.; Ju, H. L.; Moon, J. C.; Zakutayev, A.; Richard, A. P.; Russell, J.; McIntyre, D. H. Origin of p-type conduction in single-crystal $CuAlO_2$. *Phys. Rev. B: Condens. Matter Mater. Phys.* **2009**, *80* (16), 165206.
(57) Chikoidze, E.; Sartel, C.; Mohamed, H.; Madaci, I.; Tchelidze, T.; Modreanu, M.; Vales-Castro, P.; Rubio, C.; Arnold, C.; Sallet, V.; Dumont, Y.; Perez-Tomas, A. Enhancing the intrinsic p-type conductivity of the ultra-wide bandgap Ga_2O_3 semiconductor. *J. Mater. Chem. C* **2019**, *7* (33), 10231−10239.
(58) Takabatake, T.; Suekuni, K.; Nakayama, T.; Kaneshita, E. Phonon-glass electron-crystal thermoelectric clathrates: Experiments and theory. *Rev. Mod. Phys.* **2014**, *86* (2), 669−716.
(59) Acharyya, P.; Ghosh, T.; Pal, K.; Kundu, K.; Singh Rana, K.; Pandey, J.; Soni, A.; Waghmare, U. V.; Biswas, K. Intrinsically Ultralow Thermal Conductivity in Ruddlesden−Popper 2D Perovskite $Cs_2PbI_2Cl_2$: Localized Anharmonic Vibrations and Dynamic Octahedral Distortions. *J. Am. Chem. Soc.* **2020**, *142* (36), 15595−15603.
(60) Cahill, D. G.; Watson, S. K.; Pohl, R. O. Lower limit to the thermal conductivity of disordered crystals. *Phys. Rev. B: Condens. Matter Mater. Phys.* **1992**, *46* (10), 6131−6140.
(61) Agne, M. T.; Hanus, R.; Snyder, G. J. Minimum thermal conductivity in the context of diffuson-mediated thermal transport. *Energy Environ. Sci.* **2018**, *11* (3), 609−616.
(62) Allen, P. B.; Feldman, J. L.; Fabian, J.; Wooten, F. Diffusons, locons and propagons: Character of atomic vibrations in amorphous Si. *Philos. Mag. B* **1999**, *79* (11−12), 1715−1731.
(63) Bernges, T.; Peterlechner, M.; Wilde, G.; Agne, M. T.; Zeier, W. G. Analytical model for two-channel phonon transport engineering. *Mater. Today Phys.* **2023**, *35*, 101107.
(64) Gibson, Q. D.; Zhao, T.; Daniels, L. M.; Walker, H. C.; Daou, R.; Hébert, S.; Zanella, M.; Dyer, M. S.; Claridge, J. B.; Slater, B.; Gaultois, M. W.; Corà, F.; Alaria, J.; Rosseinsky, M. J. Low thermal conductivity in a modular inorganic material with bonding anisotropy and mismatch. *Science* **2021**, *373* (6558), 1017−1022.
(65) Zeier, W. G.; Zevalkink, A.; Gibbs, Z. M.; Hautier, G.; Kanatzidis, M. G.; Snyder, G. J. Thinking Like a Chemist: Intuition in Thermoelectric Materials. *Angew. Chem., Int. Ed.* **2016**, *55* (24), 6826−6841.
(66) Bhui, A.; Dutta, M.; Mukherjee, M.; Rana, K. S.; Singh, A. K.; Soni, A.; Biswas, K. Ultralow Thermal Conductivity in Earth-Abundant $Cu_{1.6}Bi_{4.8}S_8$: Anharmonic Rattling of Interstitial Cu. *Chem. Mater.* **2021**, *33* (8), 2993−3001.
(67) Long, S. O.; Powell, A. V.; Hull, S.; Orlandi, F.; Tang, C. C.; Supka, A. R.; Fornari, M.; Vaqueiro, P. Jahn−Teller Driven Electronic Instability in Thermoelectric Tetrahedrite. *Adv. Funct. Mater.* **2020**, *30* (12), 1909409.
(68) Christensen, M.; Abrahamsen, A. B.; Christensen, N. B.; Juranyi, F.; Andersen, N. H.; Lefmann, K.; Andreasson, J.; Bahl, C. R. H.; Iversen, B. B. Avoided crossing of rattler modes in thermoelectric materials. *Nat. Mater.* **2008**, *7* (10), 811−815.
(69) Koza, M. M.; Johnson, M. R.; Viennois, R.; Mutka, H.; Girard, L.; Ravot, D. Breakdown of phonon glass paradigm in La- and Ce-filled Fe_4Sb_{12} skutterudites. *Nat. Mater.* **2008**, *7* (10), 805−810.
(70) Nolas, G. S.; Cohn, J. L.; Slack, G. A.; Schujman, S. B. Semiconducting Ge clathrates: Promising candidates for thermoelectric applications. *Appl. Phys. Lett.* **1998**, *73* (2), 178−180.
(71) Nolas, G. S.; Cohn, J. L.; Slack, G. A. Effect of partial void filling on the lattice thermal conductivity of skutterudites. *Phys. Rev. B: Condens. Matter Mater. Phys.* **1998**, *58* (1), 164−170.
(72) Jiang, Y.; Jia, F.; Chen, L.; Wu, L.-M. $Cu_4Bi_4Se_9$: A Thermoelectric Symphony of Rattling, Anharmonic Lone-pair, and Structural Complexity. *ACS Appl. Mater. Interfaces* **2019**, *11* (40), 36616−36625.

https://doi.org/10.1021/acs.chemmater.4c00188
Chem. Mater. 2024, 36, 4530−4541